Biomaterials 32 (2011) 3367–3374

Contents lists available at ScienceDirect

Biomaterials

journal homepage: www.elsevier.com/locate/biomaterials

Failure of Aβ(1-40) amyloid fibrils under tensile loading

Raffaella Paparcone [a], Markus J. Buehler [a,b,*]

[a] Laboratory for Atomistic and Molecular Mechanics, Department of Civil and Environmental Engineering, Massachusetts Institute of Technology, 77 Massachusetts Ave., Room 1-235A&B, Cambridge, MA, USA
[b] Center for Computational Engineering, Massachusetts Institute of Technology, 77 Massachusetts Ave., Cambridge, MA, USA

ARTICLE INFO

Article history:
Received 3 November 2010
Accepted 26 November 2010
Available online 6 February 2011

Keywords:
Amyloid fibril
Mechanical properties
Failure
Length scale
Elasticity
Nanomechanics

ABSTRACT

Amyloid fibrils and plaques are detected in the brain tissue of patients affected by Alzheimer's disease, but have also been found as part of normal physiological processes such as bacterial adhesion. Due to their highly organized structures, amyloid proteins have also been used for the development of nanomaterials, for a variety of applications including biomaterials for tissue engineering, nanolectronics, or optical devices. Past research on amyloid fibrils resulted in advances in identifying their mechanical properties, revealing a remarkable stiffness. However, the failure mechanism under tensile loading has not been elucidated yet, despite its importance for the understanding of key mechanical properties of amyloid fibrils and plaques as well as the growth and aggregation of amyloids into long fibers and plaques. Here we report a molecular level analysis of failure of amyloids under uniaxial tensile loading. Our molecular modeling results demonstrate that amyloid fibrils are extremely stiff with a Young's modulus in the range of 18–30 GPa, in good agreement with previous experimental and computational findings. The most important contribution of our study is our finding that amyloid fibrils fail at relatively small strains of 2.5%–4%, and at stress levels in the range of 1.02 to 0.64 GPa, in good agreement with experimental findings. Notably, we find that the strength properties of amyloid fibrils are extremely length dependent, and that longer amyloid fibrils show drastically smaller failure strains and failure stresses. As a result, longer fibrils in excess of hundreds of nanometers to micrometers have a greatly enhanced propensity towards spontaneous fragmentation and failure. We use a combination of simulation results and simple theoretical models to define critical fibril lengths where distinct failure mechanisms dominate.

1. Introduction

Initially solely associated with severe disorders [1], amyloid protein materials are now recognized also as common protein structures with important biological functional roles [1–3] as bacterial coatings [1], protective materials in egg envelopes of several fish species and insects [4,5] and scaffold for catalytic reactions [6]. Amyloid protein materials often result from protein misfolding pathways that generate fibrillar aggregates with a common core structure consisting of an elongated stack of beta-strands stabilized by a dense network of hydrogen bonds [7]. This structural arrangement confers high stability and remarkable mechanical properties, which have been investigated both theoretically and experimentally [8–11]. In particular, amyloids feature a high elasticity, with Young's moduli ranging between 10 GPa and 20 GPa as well as a high bending stiffness [9,10]. According to earlier experimental and theoretical studies these mechanical properties are related to their molecular structure [10,12]. The exceptional mechanical properties of amyloids make them good candidates for a wide range of potential technological applications, and specifically as new bionanomaterials utilizing them as nanowires [13–16], gels [17–22], scaffolds and biotemplates [13,22–27], liquid crystals [28], adhesives [29] and biofilm materials [30]. These applications often imply the functionalization of the amyloid fibrils with the introduction of additional elements, including enzymes, metal ions, fluorophores, biotin or cytochromes. Amyloids have been also proposed for biological applications in cell adhesion [31] and as bioadhesives for tissue regeneration and engineering [32], on the basis that amyloid toxicity is associated with oligomeric species or pre-fibrillar intermediates rather than mature fibrils [33,34].

Measurements of the mechanical properties of amyloid fibrils and, in particular of their strength, are crucial to understand their potential and performance limits in applications, and the quest to elucidate the mechanics of amyloid protein materials has been

* Corresponding author. Center for Computational Engineering, Massachusetts Institute of Technology, 77 Massachusetts Ave., Cambridge, MA, USA. Tel.: +1 617 452 23750; fax: +1 617 324 4014.
E-mail address: mbuehler@MIT.EDU (M.J. Buehler).

0142-9612/$ – see front matter © 2010 Elsevier Ltd. All rights reserved.
doi:10.1016/j.biomaterials.2010.11.066

going on for several years. Several experimental techniques, based on the mechanical manipulation of the individual nanostructures, have been used to measure elastic modulus and strength [8,35–41] and even provided a first experimental evaluation of the failure stress in the range of 0.2–1.0 GPa [8]. Recently, other experimental works based on sonication [42] and laser-induced shock wave propagation and destruction [43] have revealed a heightened tendency to breakage, and clarified some aspects of the kinetics of proliferation of amyloid fibrils. The observed high fragility of amyloid fibrils combined with the elongation mechanism that occurs only at the tails of each fibril, explain the explosive proliferation of the amyloid fibrils observed during laser irradiation due to the increased density of fibril terminals that accelerate growth [8,43]. The understanding of proliferation mechanisms is fundamental not only for material science applications, but also for biomedicine, which faces issues related to deposition and uncontrolled self-assembly of amyloids in the form of large plaques with dimensions on the order of micrometers. They result from a hierarchical organization that, from the atomistic level reaches the nanometer scale, where one or more fibrils arrange to form protofilaments [44–46] and the assembly of multiple protofilaments results in a variety of morphologies, including twisted rope-like structures, flat-tapes with nanometer-scale diameters [47,48], spherulitic structures [49] and, at a higher level of complexity, the characteristic amyloid plaques found in affected tissues.

The understanding of the failure mechanism under tensile stress and the transfer of the mentioned brittleness over larger size scales is crucial in several application areas, including amyloid aggregate growth, the development of biomaterials, and the understanding of changes of mechanical properties across multiple material scales. To date, however, no direct tensile loading test of amyloid fibrils has been conducted. The molecular structure of the amyloid fibrils and the presence of the stabilizing hydrogen bonds network makes such tests extremely challenging from an experimental perspective, in particular pertaining to the application of load at the level of individual fibrils. Further, a systematic study of the mechanical properties of amyloid fibrils over different length scales is currently missing. This is an important issue to shed light onto the mechanism of growth of amyloid fibrils, since, despite the importance of the self-propagating nature of amyloids, many questions related to how the fibers grow and form remain open. Some experimental works suggest that amyloid growth occurs by the addition of oligomeric intermediates at fiber ends [50], while other results demonstrate that amyloids grow efficiently by the addition of monomers to fiber ends [51].

In this paper, we report a series of molecular dynamics simulations investigating the mechanical failure response of amyloid fibrils with lengths up to ≈190 Å due to direct tensile loading. The insight derived here has important implications for the development of models of larger-scale amyloid plaques where thousands of fibrils supposedly approach the micrometer scale [52] and interact determining the observed stiffness of amyloid plaques [30,53].

2. Materials and methods

2.1. Amyloid fibril geometry setup

We investigate Aβ(1-40) amyloid fibrils associated with Alzheimer's disease as a model system. The basic structure of this amyloid fibril has been determined through solid state Nuclear Magnetic Resonance (ssNMR) investigations [54]. Each fibril is characterized by a beta-cross structure, deriving from the repetition of layers stacking on top of each other and stabilized by a dense hydrogen bond network. Each layer comprises two, sequence-wise identical, U-turns (sequence: DAEFRHDSGYEVHHQKLVFFAEDVGSNKGAIIGLMVGGVV) [54,55], and is twisted by an average angle θ with respect to the nearest neighbor layers. According to the ssNMR data, the first eight residues show structural disorder [54] and the corresponding coordinates are not yet available. Therefore only the last 32 amino acids are taken into account to build the fibrils, starting from the glycine (G) at position 9. Each U-turn contains 32 alpha carbons and we will consider a number $N_c = 64$ of alpha carbons per layer. According to the adopted Cartesian representation, the fibril grows along the z axis, while the twist rotation occurs in the x-y-plane. Fibrils of $n = 20$, 30 and 40 layers are built following the method described in references [56] and [11]. Thereby the coordinates of one layer are copied and translated along the fibril axis imposing the typical beta-sheet interlayer distance (4.8 Å) and any interlayer twist rotation [56]. The length (L_n) of fibrils composed of n layers ($n = 20$, 30, 40) is evaluated as the distance between the centroids of the alpha carbons composing the top and bottom layers. The values of L_n result to be $L_{20} = 91.87$ Å, $L_{30} = 144.33$ Å and $L_{40} = 189.75$ Å for 20, 30 and 40 layers, respectively. The simulation of larger fibrils is computationally prohibitive due to the size of these larger molecular fibrils. The subsequent molecular relaxation process will drive the fibril towards the optimized interlayer distances and twist angles [56] (see next sections for details on the molecular dynamics simulation approach used in our study).

2.2. Mechanical characterization

The relaxed configuration of each amyloid fibril is extracted from the corresponding relaxation trajectory and forms the reference structure to investigate the mechanical response to applied strain. A relaxed fibril with length L_{20} is represented in the snapshot of Fig. 1A corresponding to 0% applied strain as an example. Deformed systems with applied strain are generated by homogenously rescaling the coordinates of the relaxed fibrils along the growth axis. In each case, the imposed strain (denoted by ε) ranges between 1% and a maximum value in excess of the strain where failure is observed, which determines a variation of the overall fibril length from L_n to $L_n^* = L_n(1+\varepsilon)$.

Molecular dynamics simulations are performed to relax the deformed fibrils under displacement boundary conditions. To apply displacement boundary conditions (to realize prescribed strain), the positions of the alpha carbons composing the top and the bottom layers are fixed in the axis direction, but are allowed to move freely in the plane orthogonal to the fibril axis (Fig. 1B). This allows to account for winding/unwinding rotational motions that are expected as a consequence of the molecular rearrangements at each applied load (following earlier results reported in [10]). A quantitative analysis of fibrils, carefully relaxed at each level of applied strain, is performed by averaging relevant quantities (twist, number of hydrogen bonds, energy, etc.) over the last 1 ns of relaxation, using the CHARMM molecular dynamics program [57]. The energy values reported here (e.g. in Fig. 2) are averaged over the last 1 ns relaxation and normalized by the starting volume (V) of the fibril. The volume V is evaluated as $L_n\, A_c$, being $A_c = 1414.32$ Å^2 (the cross-section area) estimated as described in earlier work [10]. The variations of the number of hydrogen bonds is calculated using the software VMD [58] by imposing a cutoff distance of 4 Å and a cutoff angle of 40°. The interlayer twist angle is evaluated by considering the position of the alpha carbons of the residue serine 26 along the sequence given above [56].

The average local displacement is a useful variable to visualize the distribution of the strain along each fibril and to gain information on the occurrence of the failure. In a fibril composed of n layers, for each layer (j) we define a local interlayer distance

$$d_j^0 = \frac{1}{N_c}\sum_{i=1}^{N_c}\left|r_{ij}^0 - r_{i(j+1)}^0\right| \tag{1}$$

where r_{ij}^0 and $r_{i(j+1)}^0$ identify the positions of the ith alpha carbon in the layer j and $j+1$, respectively, and N_c is the number of alpha-carbon atoms involved. Similarly, for each time step (k) extracted from the relaxation trajectory of the deformed fibrils, we define the local distance as

$$d_{jk} = \frac{1}{N_c}\sum_{i=1}^{N_c}\left|r_{ijk} - r_{i(j+1)k}\right| \tag{2}$$

where r_{ijk} and $r_{i(j+1)k}$ identify the positions of the ith alpha carbon in the layer j and $j+1$of the deformed fibrils at time step k, respectively. The local strain per layer and per time step, ε_{jk} is

$$\varepsilon_{jk} = \frac{d_{jk} - d_j^0}{d_j^0} \tag{3}$$

The maps shown in Fig. 4 report the values of the local strain $<\varepsilon_j>$ averaged over the last 1 ns relaxation, evaluated for each applied strain.

2.3. Molecular dynamics simulation approach

Molecular interactions are modeled on the basis of the all-atom CHARMM19 polar force field combined with an effective Gaussian model for the water solvent (EEF1) [59], where the implicit solvent model is chosen because of the size of the investigated systems. Its applicability is supported by earlier studies that compare the utilization of the explicit and implicit models [60] and validate the results against the experimental data [10,61]. The non-deformed fibrils are first minimized to relax the system to a favorable starting configuration, and then equilibrated at

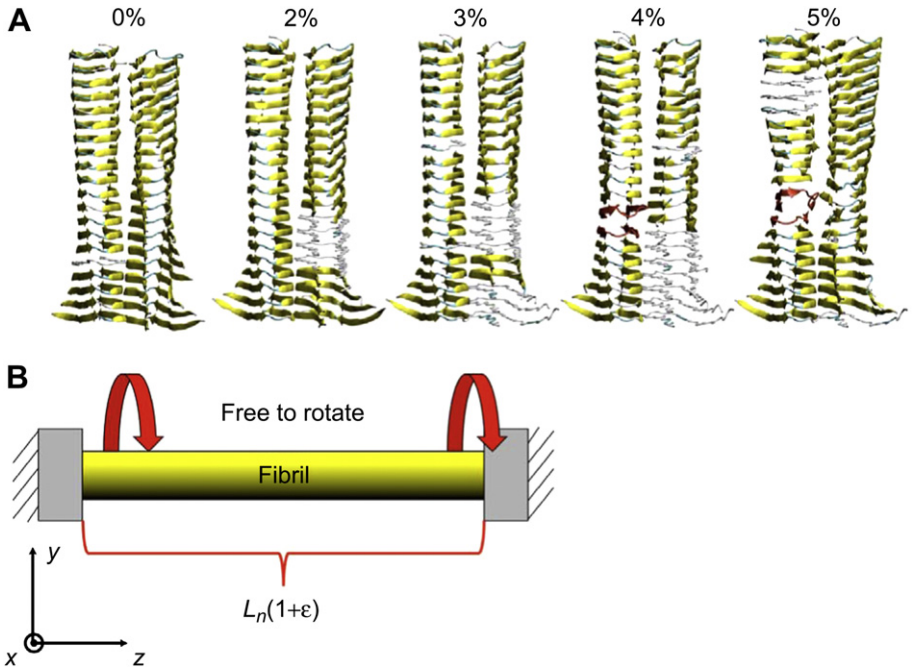

Fig. 1. Tensile testing of amyloid fibrils. A, Snapshots of the relaxed configuration of a L_{20} = 91.87 Å long amyloid fibril at the different applied stresses, indicated above each structure. The red color is used to localize the failure point. The hydrogen bond network starts featuring irregularities at 4% strain, while the real opening of the fibrils occurs only at higher strains (5%). B, Schematic representation of the loading geometry: the tails of the sample are constrained only in the directions of the fibril axis (z), while they can rotate in the x-y-plane (the x-axis is orthogonal to the y-z-plane).

constant temperature (using an *NVT* ensemble) at 300 K. The minimization consists of 10,000 Steepest Descent (SD) steps followed by 50,000 Adopted Basis Newton–Raphson Method steps. The subsequent relaxation is performed using the Velocity-Verlet algorithm (VV2) with a time step of 0.001 ps. No constraints are imposed to the system during energy minimization and relaxation. The relaxation is performed until the root mean square deviation (RMSD) of the protein structure remains constant, ensuring that convergence is achieved during the simulation. In all cases the structures are relaxed for a time of approximately 10 ns and convergence is reached. Similarly, each deformed fibril is relaxed until convergence, using the same algorithm (VV2) and time step, but position restraints are applied as described above. In all cases the required relaxation time is in the range of 10–15 ns (where the last 1 ns is taken to evaluate quantities used for the mechanical analysis).

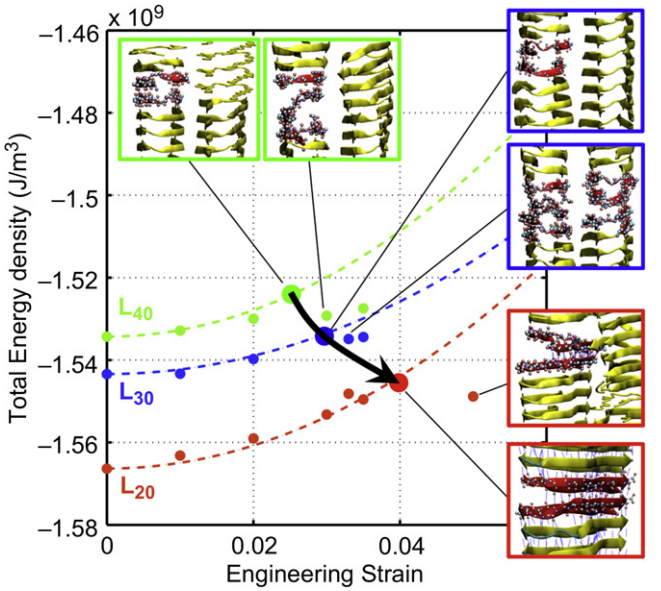

Fig. 2. Variations of the average energy density as function of the applied strain. The reported values of the total energy density for fibrils with lengths L_{20} = 91.87 Å, L_{30} = 144.33 Å and L_{40} = 189.75 Å are averaged over the last 1 ns relaxation. The reported dashed curves correspond to the fitting functions expressed by Eq. (4). In all cases the same mechanism can be observed: occurrence of a permanent defect in the fibril and failure, which consists in the evident interruption of the hydrogen bonds network. The steps of such mechanism are described by the snapshots reported as insets for each studied fibril length.

3. Results and discussion

The analysis reported in this paper has, as a primary objective, the elucidation of molecular failure mechanisms, strength properties and associated characteristic length-scale ranges where the amyloid fibril mechanical response and failure can be distinguished on the basis of its geometry. We first present the results of tensile tests with a detailed study of the molecular failure mechanisms and then proceed to report a theoretical model to explain the results used to upscale the failure properties to larger length-scales. We conclude with a discussion of the results.

3.1. Tensile tests and failure mechanism

Computational uniaxial tensile experiments are conducted on amyloid fibrils with lengths ranging between ≈92 Å and ≈190 Å (Fig. 1B). Fig. 1A shows a 91.87 Å amyloid fibril with different applied strain levels. We find that when the strain reaches the 4%, the distribution of the beta-sheets starts to show local irregularities and small defects appear along the fibril, as highlighted by the red color in the snapshots of Fig. 1A. A further increase of the strain results in the complete opening between two layers, which resembles a starting crack that drives the complete failure of the fibril as it grows. The same failure mechanism is observed in longer fibrils. In all cases, when a critical value of the applied strain (ε_1) is reached, defects in the regular distribution of the beta-sheets emerge and grow subsequently. Notably, the irregularities (insets of Fig. 2) remain stable over relatively long relaxation times (10–15 ns) and complete failure is observed only at a larger strain

$\varepsilon_2 > \varepsilon_1$. A careful analysis of the simulation trajectories suggests that these two steps defining the failure mechanism occur at different applied strains in fibrils with different lengths. More specifically, the longer the fibril, the smaller the critical strain values ε_1 and ε_2 necessary to initiate the failure process. This observation suggests a length dependence of the failure strain in tension, and as a result, a length dependence of the failure stress.

In order to define a consistent method to choose the values of ε_1 and ε_2 for different fibril lengths, we analyze the elastic potential energy (Φ) per unit volume of each relaxed system. In Fig. 2 we report the elastic energy density for each fibril length as a function of the applied strain. The three groups of data points resulting from the three amyloid fibrils studied here are each fitted using the function

$$\Phi = \Phi_0 + \frac{1}{2}E\varepsilon^2, \tag{4}$$

where E is the Young's modulus, which has been evaluated in several earlier studies by both experiments and theory [9,10]. Eq. (4) holds in the elastic deformation regime and deviations from the predicted trend indicate the starting of a failure or the occurrence of significant deformations/defects in the fibril. On the basis of these observations, fitting functions are calculated including the strain values that follow the elastic trend, before molecular failure. The points immediately before large deviations from Eq. (4) resemble the critical failure strains ε_1. The observation of the average fibril configurations reported in the insets of Fig. 2 allows to confirm the defined critical failure strains ε_1 and the corresponding values of ε_2 (Table 1). The deformed relaxed fibrils show that the deviation from the elastic trend can be observed only when a significant opening appears in the structure (and the strain level is ε_2), while the points corresponding to the simple occurrence of defects are still within the range of elasticity (strain level ε_1). The values of the elastic moduli estimated from the fitting functions reported in Fig. 2 are listed in Table 1 and allow us to calculate an average Young's modulus value $E = 25.51$ GPa that will be used in our next calculations. This value is in good agreement with the previous theoretical and experimental findings [9,10]. The values of ε_1 are represented as bigger circles in the plot of Fig. 2, and a black arrow is used to highlight their decrease with respect to the increasing fibril length. The corresponding failure stresses σ_1 are calculated via $E\varepsilon_1$ and reported in Table 1.

The analysis of the chemical and geometrical properties of the relaxed deformed fibrils provides information about the rearrangements occurring during the relaxation. In particular, the variation of the number of hydrogen bonds (Fig. 3A) shows a decrease and reveals that the imposed displacement and increase of the average interlayer distance result in a continuous decrease of the hydrogen bond network density until final failure occurs. Interestingly, the opening of the crack in the fibril corresponds to an increase of the average number of hydrogen bonds, which, even during failure, drive the response of the fibril and its subsequent rearrangement. The snapshots reported in the insets of Fig. 2 show the enhancement of the efficiency of hydrogen bonds in stabilizing the structure in this intermediate state. This is because before the ultimate failure, the failing layer rearranges between its two neighbors so that its backbone can still be involved in hydrogen bonding interactions with both the upper and the lower U-turns. This rearrangement drives the formation of two connected compact subfibrils, explaining the increase of the number of hydrogen bonds. The observed rearrangement mechanism suggests that the minimum number of hydrogen bonds is reached immediately before the occurrence of the failure, and the minimum of the fitting curves used in Fig. 3A gives us another, independent estimation of the critical failure strains for each fibril length. In the plot of Fig. 3A, the bigger circles correspond to the values of the critical strain ε_1 determined on the basis of energy density evaluation (Fig. 2), while in Fig. 3B, a comparison between these values and the ones determined from the analysis of the variation of the hydrogen bonds, is shown. Despite small differences, both analysis methods independently lead to quite similar values of the critical failure strain, and most importantly, confirm the effect of the fibril length on the required strain to reach failure.

Previous works have demonstrated the importance of the twist angle combined with the overall molecular rearrangement occurring during the loading. A coupling between the tension/compression and the winding/unwinding has been observed and considered has a key player in driving the relatively high mechanical stability of the Aβ amyloid fibrils [10,62]. The analysis of the interlayer twist angle variations at each applied strain is reported in Fig. 3C. As already observed in earlier simulation work in the solely elastic regime [10], the tensile test is accompanied by an unwinding process, which determines a decrease of the average interlayer twist angle. When the fibril fails, the formation of two connected subfibrils implies the reduction of the constraints imposed by the applied strain and a subsequent return to the optimized molecular distances and angles. This internal reorganization results in a sudden increase of the twist angle (represented by the arrows in Fig. 3C) that tends to reach the optimal value of the relaxed, starting non-deformed configuration.

The analysis of the energy density variations, number of hydrogen bonds and interlayer twist angle, provides consistent information about the effect of the fibril length on the occurrence of the failure and the required critical strain. The strain maps reported in Fig. 4 show the local strain along each fibril at the different applied strains. The values reported in the maps resemble the average over the alpha carbons composing each layer and over the last 1 ns relaxation (for details see Materials and methods). The averaging allows for a visual comparison of the effect of a certain applied strain on different parts of the same fibril or on fibrils having a different length. From the observation of the maps reported in Fig. 4, it is evident that an applied strain of 2.5% has a significant effect only when the fibril length reaches ≈ 190 Å, that is, 40 layers, while there is no relevant variation in shorter fibrils. Similarly a 4% strain is needed to visualize an actual failure of the shortest analyzed fibril (≈ 92 Å). Moreover, the calculation of the local strain along each fibril is a powerful tool to confirm that the used strain boundary conditions prevent the localization of the strain at the boundaries, providing a valid method to investigate the failure of these amyloid fibrils under tensile loading. The choice of using strain boundary conditions is dictated by the intrinsic issues related to alternative techniques, as steered molecular dynamics or the application of constant forces, which imply an external load directly on the atoms composing the layers of the fibril terminals. The absence of covalent bonds linking one layer to the other does not allow a homogenous distribution of the energy transferred during the

Table 1
Young's moduli, critical strains (ε_1 and ε_2) and strength (σ_1) of the amyloid fibrils studied in this paper. The Young's moduli E_n are calculated from the fitting functions (Eq. (4)) reported in Fig. 2 and the subscript n distinguishes the fibrils on the basis of their length ($n = 20$, 30 or 40 layers). The parameter ε_1 represents the critical strain corresponding to the occurrence of permanent and stable defects in the fibril, and ε_2 is a strain value that already implies the failure of the fibril and causes a deviation of the energy of the system from the predicted trend in the elastic regime (Fig. 2). The strength values are calculated as $\sigma_1 = E\varepsilon_1$.

	91.87 Å (20 layers)	144.33 Å (30 layers)	189.75 Å (40 layers)
E_n (GPa)	28.06	18.04	30.42
ε_1	0.04	0.03	0.025
ε_2	0.05	0.033	0.03
σ_1 (GPa)	1.02	0.76	0.64

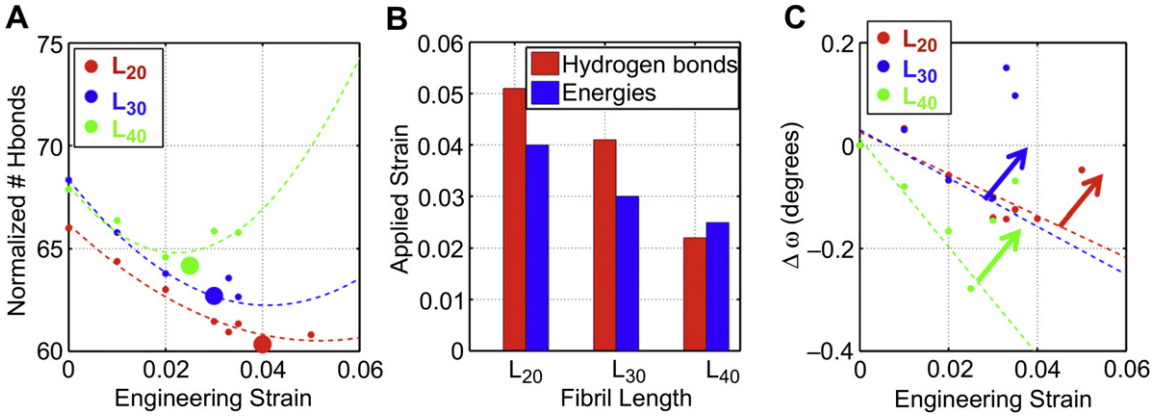

Fig. 3. Geometrical and chemical variation during the failure in tension. A, Normalized number of hydrogen bonds as a function of the applied strain for fibrils having length of $L_{20} = 91.87$ Å, $L_{30} = 144.33$ Å and $L_{40} = 189.75$ Å. The failure is here highlighted by the deviation of the data points from the initial trend. The longer the fibril, the larger the deviation: in particular the longest fibril shows a significant increase of the hydrogen bonds number, which can be justified considering the formation of two compact sub-fibrils when the failure occurs. The bigger circles identify the strain critical values obtained from the energy analysis (ε_1) (see Fig. 2). B, Comparison between the failure strains ε_1 and the corresponding values calculated as the minima of the fitting functions of the hydrogen bonds variations. C, Variation of the interstrand twist angle measured during the loading. As in the case of the hydrogen bonds, failure causes a deviation (represented using the arrows) from the starting, linear trend. This finding shows the tendency of the fibril to return its original interstrand twist angle, which has been previously perturbed by the applied strain.

loading, and thus, the subsequent localization of the strain would result in the failure of the top layer without giving any useful information about the failure strain and the corresponding mechanism. In this context the strain boundary conditions used here represent an efficient way to test the mechanical properties (and in particular the failure) in tension of the fibrils.

3.2. Size effect of the failure of amyloid fibrils

The results presented in the previous section show that there exists a length dependence of the failure strain of amyloid fibrils subjected to uniaxial tension. A closer inspection of the mechanism suggests that at this level, the displacement plays a key role in determining the failure of the fibril. In this range of lengths the same applied strain results in an average displacement significantly different from one fibril length to another, *i.e.* a higher displacement is measured in longer fibrils thus explaining their increased weakness with respect to shorter ones. This finding can be directly explained based on a simple model. Let us assume that for a fibril of any length, the minimum displacement required for the failure corresponds to a critical value $D_{cr} = 4.8$ Å, which is assumed to be the typical interlayer average distance in beta-sheet secondary structures. In light of this simple model this distance represents the minimum displacement required to introduce an additional layer in the failure crack of the fibril (Fig. 5). In the elastic regime, the failure force (F_{cr}) required to reach the critical displacement in a fibril of length L_n and cross-section area A_c is

$$F_{cr} = \frac{A_c E D_{cr}}{L_n} \tag{5}$$

and the corresponding critical strain ε_{cr} is:

$$\varepsilon_{cr} = \frac{D_{cr}}{L_n} \tag{6}$$

In Fig. 6A, the values of F_{cr} and $\sigma_{cr} = E\varepsilon_{cr}$ are reported as a function of the fibril length. The failure stress and the failure force profiles overlap in the reported ranges and show a strong length dependence for short fibrils. In the same plot the values of the critical stresses, σ_1 (see Table 1) measured for each studied fibril length using computational experiments, are reported and compared with the predicted values (σ_{cr}). The good agreement suggests that the fibril lengths investigated in this paper fall in a length scale where the required failure force and the corresponding strain are still strongly affected by the length of the fibril, and that the failure is controlled by the displacement. The trends of the predicted failure force and stress reported in Fig. 6A show that

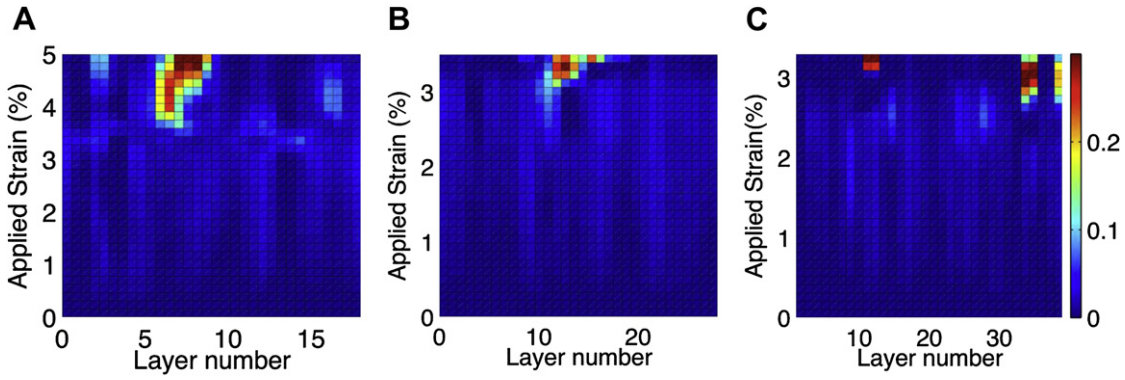

Fig. 4. Average local strain distribution during the tensile loading. The local strain $<\varepsilon_j>$ is calculated considering the average distance between each layer and its neighbor along the fibril axis, as explained in the Materials and Methods section. The values reported in panels A, B, and C correspond to the local strains averaged over the last 1 ns relaxation at different applied strain for the fibrils having lengths of 91.87 Å, 144.33 Å and 189.75 Å respectively.

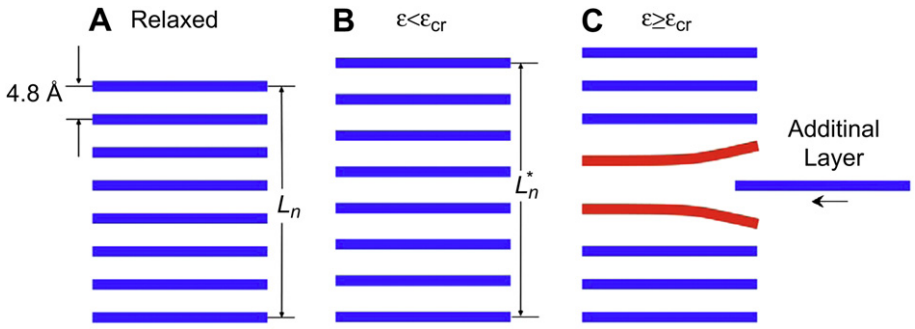

Fig. 5. Schematic representation of the simple model used here to describe the failure condition of an amyloid fibril under the application of external strain. A, Simple relaxed fibril composed of equispaced layers and having length L_n. B, Deformed fibril having length of $L_n^* = L_n(1+\varepsilon)$. The applied strain ε is smaller than the critical value ε_{cr} and the displacement is equally distributed along the fibril. C, Amyloid fibril at applied strain $\varepsilon > \varepsilon_{cr}$. The reached displacement approaches the value of $D_{cr} = 4.8$ Å and the subsequent localization causes failure of the fibril.

the fibril length effect tends to vanish for increasing fibril lengths, approaching zero for infinitely long fibrils.

However, according to a previous theoretical work [63] a value of $F_{ref} = 175 \pm 125$ pN has been proposed as a minimum failure force required to break a dense hydrogen cluster bonded protein structure. Combined with the observation of the trends reported in Fig. 6A failure is controlled by the displacement only until the failure force approaches the critical value of F_{ref}. This is highlighted in Fig. 6 by dashed grey lines defining the corresponding ranges. Such force values corresponds to a failure stress $\sigma_{ref} = F_{ref}/A_c$, ranging between 0.0035 and 0.021 GPa and to a strain ε_{ref} varying from 0.014% to 0.084%. This force and stress level is reached for fibril length L_{ref} in the range 576–3430 nm (Eq. (5)) and, specifically $L_{ref} = 986$ nm (around one micrometer), for $F_{ref} = 175$ pN. This length scale defines the occurrence of a transition in the failure controlling mechanisms, where fibrils longer than L_{ref} are predicted to show a failure strength that is independent of their length. Fig. 6B zooms into the range 0.1–10 μm and highlights the mentioned transition of the failure mechanisms. This result is quite interesting especially considering that the found critical value of L_{ref} is far smaller than the amyloid fibrils persistence length that has been estimated in experiment and simulation as ranging between 6 and 48 μm [8,10]. In Fig. 7, a summary of the most relevant length scales defining the mechanical behavior of amyloid fibrils is reported, along with the corresponding failure stresses in GPa. The length scale is characterized by a displacement controlled and thus length-dependent failure strength in tension, and includes the range investigated in this paper through our direct computational experiments ($L_{20} = 9.2$ nm, $L_{30} = 14.43$ nm and $L_{40} = 18.97$ nm). The length-scale of 120 nm corresponds to the helical pitch of the amyloid fibrils and represents a geometrical feature of amyloid fibrils. When the length of the fibrils approaches L_{ref} the failure stress is independent of the length of the fibrils [63]. We note that the failure of micrometer scale amyloid fibrils has been experimentally studied by AFM bending experiments [8] and by sonication [42]. In both cases, the estimated strength is in the range 0.1–1.1 GPa, in agreement with the predictions made in our simulations. However, an experimental validation for the length dependence and in particular the reaching of the asymptotic strength beyond L_{ref} remains outstanding. We note also that the increasing weakness of longer protein filaments has also been observed in previous works on alpha helices, for example [64,65]. The importance of amyloid fibril fragmentation for growth and aggregation has been experimentally demonstrated also by laser-induced destruction of amyloid β fibrils, which resulted in an explosive propagation of the formation of a larger number of fibrils and plaque formation [43]. The occurrence of enhanced breakage processes increases the density of the ends at which the growth occurs and favors the proliferation of new fibrils. These observations can have important implications not only in the understanding of the progress of

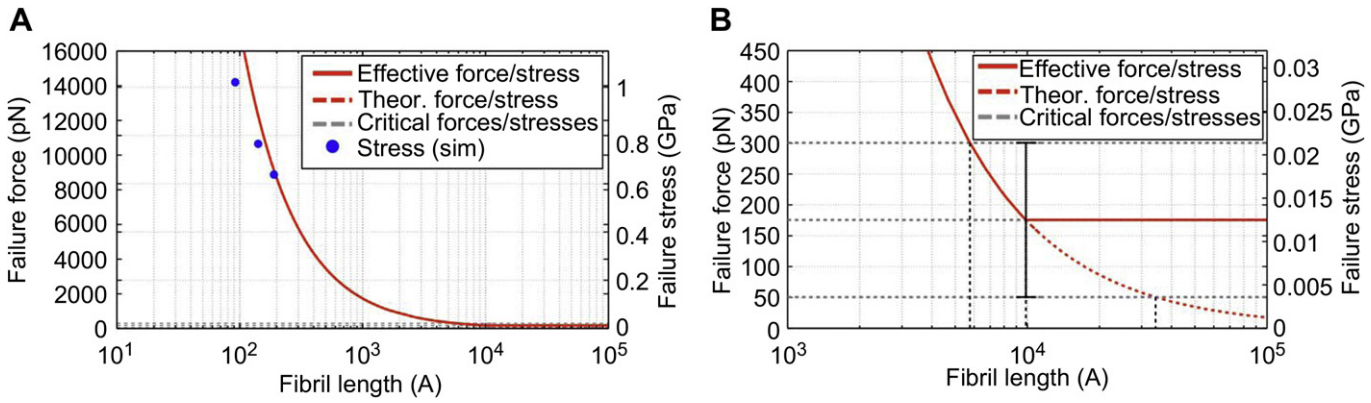

Fig. 6. Failure force and failure stress for fibrils with length reaching the micrometer scale. A, Values of predicted force (F_{cr}) and stress (σ_{cr}). The plot shows also a comparison of the predicted failure stress (σ_{cr}) with the values measured using atomistic simulations, σ_1 (Table 1). The good agreement shows that the studied fibril lengths lay in the length scale where the failure in tension is controlled by the displacement. B, As in A, failure force and stress are reported as function of the fibril lengths. This plot zooms into the range 0.1–10 μm and highlights the force and stress ranges defining the transition of the failure mechanisms. In both panels, the grey dashed lines correspond to the failure force and stress ranges, around $F_{ref} = 175 \pm 125$ pN and failure stress (σ_{ref}) ranging between 0.0035 and 0.021 GPa. The corresponding strain (ε_{ref}) varies between 0.08% and 0.014%. The theoretical prediction of a failure in tension driven by the displacement (red dashed line) is valid until the failure force/stress reaches the corresponding critical range and a fibril length between 576 and 3430 nm, as shown by the vertical dashed black lines in the plot.

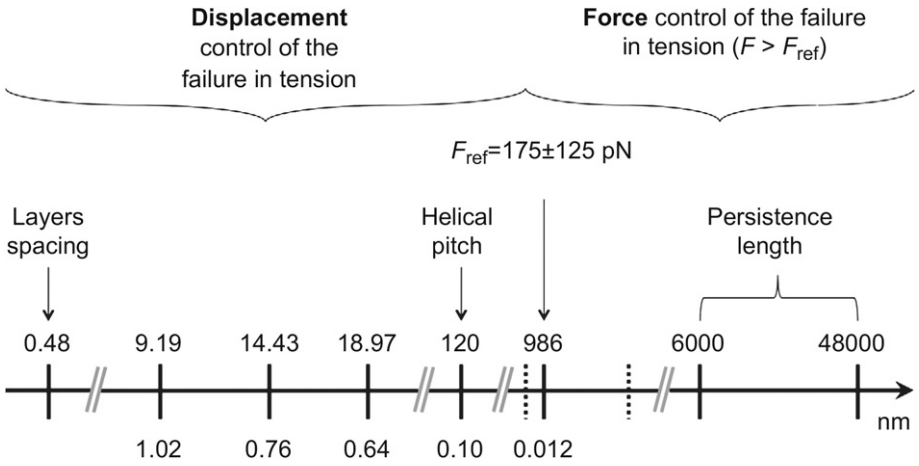

Fig. 7. Amyloid fibril lengths and corresponding strengths. The mechanical response of an amyloid fibril under tensile loading is strongly dependent on its length. On the basis of theoretical and computational results, we can define a distinction of different length scales, where the fibril mechanical behavior is driven by different factors. Along the represented nanometer scale, we define the layer spacing [7], which implies the least displacement required to introduce an additional layer in the fibril and the lengths of the fibrils studied in this paper (L_{20} = 9.19 nm, L_{30} = 14.43 nm and L_{40} = 18.97 nm). 120 nm corresponds to the helical pitch and to a mechanical response mainly dominated by twist effects [12]. The corresponding failure stresses are also reported in GPa. They show the decrease of the required maximal stress with the increasing length. The value of F_{ref} = 175 ± 125 pN represents the minimum force required to break a hydrogen bond cluster stabilized protein fibril [63]. The identified critical fibril length range (dashed black lines) around L_{ref} = 986 nm defines the transition in the failure mechanism: Fibrils shorter than L_{ref} experience a displacement controlled failure under tensile loading, while fibrils longer than L_{ref} can fail with the only condition that the applied force is larger than F_{ref} [63].

neurodegenerative diseases, but also in the development of biomaterials based on amyloids, which should be mechanically robust [42]. The results discussed here also give important insights into the mechanical performance of amyloid individual fibrils, in the context of their possible application in nanotechnology, and in light of key deformation and failure mechanisms at the molecular scale.

4. Conclusions

Our study showed that individual amyloid fibrils tend to be stiff but brittle mechanical elements, and that amyloid fibrils with longer lengths become increasingly weak and brittle. The analysis allows us to understand and predict the mechanical response of amyloid fibrils under extreme conditions. We specifically find that amyloid fibrils approaching the micrometer length-scale are mechanically weak elements, exhibiting an inherent tendency to break, perhaps even under thermal fluctuations, and thus potentially explaining the significant contributions of fragmentation mechanisms to the kinetics of fibril growth.

Acknowledgments

This research was supported by the Office of Naval Research (grant # NN00014-08-1-0844). The authors declare no conflict of interest of any sort. All authors have contributed equally to the research and the writing of this paper.

Appendix

Figures with essential color discrimination. Figs. 1–6 in this article are difficult to interpret in black and white. The full color images can be found in the online version, at doi:10.1016/j.biomaterials.2010.11.066.

References

[1] Chiti F, Dobson CM. Protein misfolding, functional amyloid, and human disease. Annu Rev Biochem 2006;75:333–66.
[2] Fowler DM, Koulov AV, Balch WE, Kelly JW. Functional amyloids: from bacteria to humans. Trends Biochem Sci 2007;32:217–24.
[3] Tanaka M, Collins SR, Toyama BH, Weissman JS. The physical basis of how prion conformations determine strain phenotypes. Nature 2006;442:585–9.
[4] Podrabsky JE, Carpenter JF, Hand SC. Survival of water stress in annual fish embryos: dehydration avoidance and egg envelope amyloid fibers. Am J Physiol-Reg I 2001;280:R123–31.
[5] Iconomidou VA, Vriend GA, Hamodrakas SJ. Amyloids protect the silkmoth oocyte and embryo. FEBS Lett 2000;479:141–5.
[6] Fowler DM, Koulov AV, Alory-Jost C, Marks MS, Balch WE, Kelly JW. Functional amyloid formation within mammalian tissue. PLOS Biol 2005;4(1).
[7] Nelson R, Sawaya MR, Balbirnie M, Madsen AO, Riekel C, Grothe R, et al. Structure of the cross-beta spine of amyloid-like fibrils. Nature 2005;435:773–8.
[8] Smith JF, Knowles TPJ, Dobson CM, Welland ME. Characterization of the nanoscale properties of individual amyloid fibrils. P Natl Acad Sci USA 2006;43(103):15806–11.
[9] Knowles TP, Fitzpatrick AW, Meehan S, Mott HR, Vendruscolo M, Dobson CM, et al. Role of intermolecular forces in defining properties of protein nanofibrils. Science 2007;318(5858):1900–2.
[10] Paparcone R, Keten S, Buehler MJ. Atomistic simulation of nanomechanical properties of Alzheimer's Abeta(1-40) amyloid fibrils under compressive and tensile loading. J Biomech 2010;43(6):1196–201.
[11] Paparcone R, Buehler MJ. Microscale structural model of Alzheimer's Abeta (1-40) amyloid fibril. Appl Phys Lett 2009;94:243904.
[12] Xu Z, Paparcone R, Buehler MJ. Alzheimer's Aβ(1-40) amyloid fibrils feature size dependent mechanical properties. Biophys J 2010;98:2053–62.
[13] Scheibel T, Parthasarathy R, Sawicki G, Lin X-M, Jaeger H, Lindquist SL. Conducting nanowires built by controlled self-assembly of amyloid fibers and selective metal deposition. P Natl Acad Sci USA 2003;100(8):4527–32.
[14] Perutz MF, Finch JT, Berriman J, Lesk A. Amyloid fibers are water filled nanotubes. P Natl Acad Sci USA 2002;99:5591–5.
[15] Lu K, Jacob J, Thiyagarajan P, Conticello VP, Lynn DG. Exploiting amyloid fibril lamination for nanotube self-assembly. J Am Chem Soc 2003;125(21):6391–3.
[16] Reches M, Gazit E. Casting metal nanowires within discrete self-assembled peptide nanotubes. Science 2003;300:625–7.
[17] Aggeli A, Bell M, Boden N, Keen JN, Knowles PF, McLeish TCB, et al. Responsive gels formed by the spontaneous self-assembly of peptides into polymeric bold beta-sheet tapes. Nature 1997;386:259–62.
[18] Aggeli A, Bell M, Carrick LM, Fishwick CWG, Harding R, Mawer PJ, et al. pH as a trigger of peptide beta-sheet self-assembly and reversible switching between nematic and isotropic phases. J Am Chem Soc 2003;125(32):9619–28.
[19] Zhang S. Fabrication of novel biomaterials through molecular self-assembly. Nat Biotechnol 2003;21:1171–8.
[20] Yang ZM, Liang GL, Wang L, Xu B. Using a kinase/phosphatase switch to regulate a supramolecular hydrogel and forming the supramolecular hydrogel in vivo. J Am Chem Soc 2006;128(9):3038–43.
[21] Mahler A, Reches M, Rechter M, Cohen S, Gazit E. Rigid, self-assembled hydrogel composed of a modified aromatic dipeptide. Adv Mater 2006;18:1365–70.
[22] Reches M, Gazit E. Biological and chemical decoration of peptide nanostructures via biotin-avidin interaction. J Nanosci Nanotechno 2007;7:2239–45.
[23] Carny O, Shalev DE, Gazit E. Fabrication of coaxial metal nanowires using self-assembled peptide nanotube scaffold. Nano Lett 2006;6:1594–7.

[24] Song Y, Challa SR, Medforth CJ, Qiu Y, Watt RK, Pena DA, et al. Synthesis of peptide-nanotube platinum-nanoparticle composites. Chem Commun 2004:1044–5.
[25] Baxa U, Speransky V, Steven AC, Wickner RB. Mechanism of inactivation on prion conversion of the Saccharomyces cerevisiae Ure2 protein. P Natl Acad Sci USA 2002;99:5253–60.
[26] Baldwin AJ, Bader R, Christodoulou J, MacPhee CE, Dobson CM, Barker PD. Cytochrome display on amyloid fibrils. J Am Chem Soc 2006;128(7):2162–3.
[27] Yemini M, Reches M, Risphon J, Gazit E. Novel electrochemical biosensing platform using self-assembled peptide nanotubes. Nano Lett 2005;5:183–6.
[28] Corrigan A, Mueller C, Krebs M. The formation of nematic liquid crystal phases by hen lysozyme amyloid fibrils. J Am Chem Soc 2006;128(46):14740–1.
[29] Mostaert AS, Higgins MJ, Fukuma T, Rindi F, Jarvis SP. Nanoscale mechanical characterisation of amyloid fibrils discovered in a natural adhesive. J Biol Phys 2006;32:393–401.
[30] Knowles TPJ, Oppenheim TW, Buell AK, Chirgadze DY, Welland ME. Nanostructured films from hierarchical self-assembly of amyloidogenic proteins. Nat Nanotechnol 2010;5:204–7.
[31] Gras SL, Tickler AK, Squires AM, Devlin GL, Horton MA, Dobson CM, et al. Functionalised amyloid fibrils for roles in cell adhesion. Biomaterials 2008;29 (11):1553–62.
[32] Kasai S, Ohga Y, Mochizuki M, Nishi N, Kadoya Y, Nomizu M. Multifunctional peptide fibrils for biomedical materials. Biopolymers 2004;76:27–33.
[33] Bucciantini M, Giannoni E, Chiti F, Baroni F, Formigli L, Zurdo JS, et al. Inherent toxicity of aggregates implies a common mechanism for protein misfolding diseases. Nature 2002;416(6880):483–4.
[34] Mucke L, Masliah E, Yu GQ, Mallory M, Rockenstein EM, Tatsuno G, et al. High-level neuronal expression of Abeta(1-42) in wild-type human amyloid protein precursor transgenic mice: synaptotoxicity without plaque formation. J Neurosci 2000;20:4050–8.
[35] Guzman C, Jeney S, Kreplak L, Kasas S, Kulik AJ, Aebi U, et al. Exploring the mechanical properties of single vimentin intermediate filaments by atomic force microscopy. J Mol Biol 2006;360:623–30.
[36] Yang L, van der Werf KO, Fitié CFC, Bennink ML, Dijkstra PJ, Feijen J. Mechanical properties of native and cross-linked type I collagen fibrils. Biophys J 2008;94 (6):2204–11.
[37] Salvetat JP, Briggs GAD, Bonard JM, Bacsa RR, Kulik AJ. Elastic and shear moduli of single-walled carbon nanotube ropes. Phys Rev Lett 1999;82:944.
[38] Durkan C, Ilie A, Saifullah MSM, Welland ME. The mechanics of nanosprings: stiffness and Young's modulus of molybdenum-based nanocrystals. Appl Phys Lett 2002;80:4244–6.
[39] Wong EW, Sheehan PE, Lieber CM. Nanobeam mechanics: elasticity, strength, and toughness of nanorods and nanotubes. Science 1997;277(5334):1971–5.
[40] Kis A, Kasas S, Babić B, Kulik AJ, Benoît W, Briggs GAD, et al. Nanomechanics of microtubules. Phys Rev Lett 2002;82:248101–4.
[41] Yu M-F, Lourie O, Dyer MJ, Moloni K, Kelly TF, Rodney RS. Strength and breaking mechanism of multiwalled carbon nanotubes under tensile load. Science 2000;287:637–40.
[42] Huang YY, Knowles TPJ, Terentjev EM. Strength of nanotubes, filaments, and nanowires from sonication-induced scission. Adv Mater 2009;21:3945–8.
[43] Yagi H, Ozawa D, Sakurai K, Kawakami T, Kuyama H, Nishimura O, et al. Laser-induced propagation and destruction of amyloid fibrils. J Biol Chem 2010;285 (25):19660–7.
[44] Jimenez JL, Nettleton EJ, Bouchard M, Robinson CV, Dobson CM, Saibil HR. The protofilament structure of insulin amyloid fibrils. P Natl Acad Sci USA 2002; 99:9196–201.
[45] Jimenez JL, Guijarro JI, Orlova E, Zurdo J, Dobson CM, Sunde M, et al. Cryo-electron microscopy structure of an SH3 amyloid fibril and model of the molecular packing. EMBO J 1999;18:815–21.
[46] Serpell LC, Sunde M, Benson MD, Tennent GA, Pepys MB, Fraser PE. The protofilament substructure of amyloid fibrils. J Mol Biol 2000;300:1033–9.
[47] Knowles TPJ, Smith JF, Craig A, Dobson CM, Welland ME. Spatial persistence of angular correlations in amyloid fibrils. Phys Rev Lett 2006;96:238301.
[48] Aggeli A, Nyrkova IA, Bell M, Harding R, Carrick L, McLeish TC, et al. Hierarchical self-assembly of chiral rod-like molecules as a model for peptide β-sheet tapes, ribbons, fibrils, and fibers. P Natl Acad Sci USA 2001;98:11857–62.
[49] Krebs MRH, MacPhee CE, Miller AF, Dunlop IE, Dobson CM, Donald AM. The formation of spherulites by amyloid fibrils of bovine insuline. P Natl Acad Sci USA 2004;101:14420–4.
[50] Serio TR, Cashikar AG, Kowal AS, Sawicky GJ, Moslehi JJ, Serpell L, et al. Nucleated conformational conversion and the replication of conformational information by a prion determinant. Science 2000;289:1317–21.
[51] Collins SR, Douglass AD, Vale RD, Weissman JS. Mechanism of prion propagation: amyloid growth occurs by monomer addition. PLOS Biol 2004;2:1582–90.
[52] Stine WB, Dahlgren KN, Krafft GA, LaDu MJ. In vitro characterization of conditions for amyloid-beta peptide oligomerization and fibrillogenesis. J Biol Chem 2003;278:11612–22.
[53] Lulevich V, Zimmer CC. Hong H-s, Jin L-w, Liu G-y. Single-cell mechanics provides a sensitive and quantitative means for probing amyloid-beta peptide and neuronal cell interactions. P Natl Acad Sci USA 2010;107(31):13872–7.
[54] Petkova AT, Ishii Y, Balbach JJ, Anzutkin ON, Leapman RD, Delaglio F, et al. A structural model for Alzheimer's beta-amyloid fibril based on experimental constraints from solid state NMR. P Natl Acad Sci USA 2002;99(26):16742–7.
[55] Ma B, Nussinov R. Stabilities and conformations of Alzheimer's beta-amyloid peptide oligomers (Abeta 16-22, Abeta 16-35, and Abeta 10-35): sequence effects. P Natl Acad Sci USA 2002;99:14126–31.
[56] Paparcone R, Sanchez J, Buehler MJ. Comparative study of polymorphous Alzheimer's Aβ(1-40) amyloid nanofibrils and microfibers. J Computational Theor Nanoscience 2010;7:1279–86.
[57] Brooks BR, Bruccoleri RE, Olafson BD, States DJ, Swaminathan S. Karplus. M. CHARMM: a program for macromolecular energy, minimization, and dynamics calculations. J Comp Chem 1983;4(2):187–217.
[58] Humphrey W, Dalke A, Schulten K. VMD - Visual molecular dynamics. J Molec Graphics 1996;14:33–8.
[59] Lazaridis T, Karplus M. Effective energy function for proteins in solution. Proteins: Struct Funct Bioinform 1999;35(2):133–52.
[60] Qin Z, Buehler MJ. Structure and dynamics of human vimentin intermediate filament dimer and tetramer in explicit and implicit solvent models. J Mol Model 2010.
[61] Qin Z, Kreplak L, Buehler MJ. Hierarchical structure controls nanomechanical properties of vimentin intermediate filaments. PLoS ONE 2009;4(10).
[62] Paparcone R, Buehler MJ. Failure of Alzheimer's Aβ(1-40) amyloid nanofibrils under compressive loading. JOM 2010;62(4):64–8.
[63] Keten S, Buehler MJ. Asymptotic strength limit of hydrogen bond assemblies in proteins at vanishing pulling rates. Phys Rev Lett 2008;100:198301.
[64] Bertaud J, Hester J, Jimenez DD, Buehler MJ. Energy landscape, structure and rate effects on strength properties of alpha-helical proteins. J Phys-Condens Mat 2010;22: paper # 035102.
[65] Qi HJ, Ortiz C, Boyce MC. Mechanics of biomacromolecular networks containing folded domains. J Eng Mater-T ASME 2006;128:509–18.